Journal of *Marine Science and Engineering*

MDPI

Article

Numerical Study of the Force Characteristics and Flow Field Patterns of a Cylinder in the Internal Solitary Wave

Miao Zhang [1], Haibao Hu [1,*], Abdellatif Ouahsine [2], Peng Du [1,3,*], Xiao Huang [1] and Luo Xie [1]

[1] School of Marine Science and Technology, Northwestern Polytechnical University, 127 Youyi Road, Beilin, Xi'an 710072, China; zhangmiao@mail.nwpu.edu.cn (M.Z.); huangxiao@nwpu.edu.cn (X.H.); xieluo@nwpu.edu.cn (L.X.)
[2] Laboratoire Roberval, Sorbonne Université, Université de Technology de Compiègne, Centre de Recherches Royallieu, CS 60319, CEDEX, 60203 Compiègne, France; ouahsine@utc.fr
[3] Xi'an Tianhe Defense Technology Co., Ltd., 158 Xibudadao Road, Gaoxin, Xi'an 710119, China
* Correspondence: huhaibao@nwpu.edu.cn (H.H.); dupeng@nwpu.edu.cn (P.D.)

Abstract: The density of the ocean is unevenly distributed along the depth direction, showing a stratified structure. When there is an external disturbance, large-scale internal solitary waves are easily generated. The internal solitary waves are bounded by the intermediate pycnocline, and the currents in the upper and lower layers will flow in opposite directions. This generates strong shear forces that threaten the safety of marine structures. In this paper, the flow field distribution characteristics of a cylinder under the action of internal solitary waves at different scales are analyzed as a research object. The whole cylinder is discretized into 40 regions, and the horizontal force applied to each section of the cylinder is extracted. The force characteristics of the cylinder are analyzed. It is concluded that the pressure is the main factor determining the magnitude of the total combined force. In addition, the paper extracts the main flow structures from the modal decomposition point of view and explains the reasons affecting the force behavior of the cylinder.

Keywords: internal solitary waves; force; cylinder; modal decomposition

Citation: Zhang, M.; Hu, H.; Ouahsine, A.; Du, P.; Huang, X.; Xie, L. Numerical Study of the Force Characteristics and Flow Field Patterns of a Cylinder in the Internal Solitary Wave. *J. Mar. Sci. Eng.* **2024**, *12*, 906. https://doi.org/10.3390/jmse12060906

Academic Editors: Angelo Rubino and Lev Shemer

Received: 15 April 2024
Revised: 18 May 2024
Accepted: 27 May 2024
Published: 29 May 2024

1. Introduction

Differences in temperature and salinity cause the density of the ocean to be distributed differently among the depth layers. When there are external disturbances, such as currents and the motion of ships, the interfaces between the layers are easily disturbed, causing fluctuations. These fluctuations are called internal solitary waves (ISWs). The ISW has a pycnocline as its interface, above and below which the current flows in the opposite direction. This produces strong underwater shear effects, like a "big pair of scissors", that threaten the safety of marine structures [1]. In addition, ISWs are characterized by large amplitude, high energy, difficult to dissipate, and widely distributed throughout the world's oceans. This indicates that the encounter of marine structures with ISWs is frequent and dangerous. Therefore, it is of great engineering value to conduct research on the forces acting on marine structures under the action of ISWs [2].

Cylinders are the basic component form of offshore structures such as Spar, columns of tension-leg platform (TLP), and deep-sea oil drilling rigs [3]. Therefore, understanding the flow field characteristics of cylinders in ISWs is of great importance for the smooth operation of offshore oil and gas development projects. To this end, Wei et al. [4] fabricated a wavemaker capable of generating nonlinear large-amplitude ISWs in a large-section stratified liquid tank. The interaction characteristics between ISWs and cylinders were revealed by accurately measuring the small changes in the ISW force applied to the cylinders in the tank. Wang et al. [5] carried out experiments related to the action of ISWs on vertical cylinders in a stratified-flow tank. The effect of wave amplitude on the flow field characteristics of the cylinder was investigated. Wang et al. [6] studied the pressure

distribution around the cylinder under the action of ISWs by means of a large eddy simulation method. It was revealed that vortex is an important factor affecting the pressure resistance of the cylinder in the ISW.

In addition to understanding the flow field distribution characteristics of the cylinder in ISWs, it is also important to be able to accurately calculate the loads exerted on the cylinder by ISWs to ensure the safety of marine structures. Cai et al. [7] introduced the Morison formula and gave the empirical coefficients in the Morison formula based on the surface wave theory. In their paper, they calculated the ISW on the vertical cylindrical horizontal force and its moment, which showed the non-negligible effect of ISW on the vertical cylinder. Thereafter, Song et al. [8] investigated the kinematic response of the cylinder under the action of ISWs based on the KDV theory in combination with the Morison formula. LÜ et al. [9] simulated the motion response of a vertical cylinder encountering different background parabolic currents. The forces on the vertical cylinder during the process were calculated using the Morison formula.

In all of the above studies, the overall forces on a whole cylinder through the depth of water or with a large draft were analyzed. However, due to the different flow characteristics at different depths, especially in different layers, there may be some differences in the force characteristics of the cylinder along the depth direction. These differences are crucial when we go to analyze the dynamic response of ISWs traversing the cylinder. Therefore, scholars have carried out studies on the force characteristics of columns located at different depths. Si et al. [10] used the generalized KdV (GKdV) model to obtain the vertical distribution of the horizontal force acting on the cylinder by a large amplitude ISW. They pointed out that the shear force reaches its maximum at the inflection point of the horizontal flow velocity. Wang et al. [11] measured the hydrodynamic coefficients of each cylinder section based on the experimental method. The paper suggested that different empirical coefficients should be used when calculating the ISW forces in different layers of the structural section. Yu et al. [12] calculated, compared, and analyzed the interactions between ISWs and a vertical cylinder using numerical simulations using the eKdV equations as the initial and boundary conditions. They divided the whole cylinder into six segments and analyzed the force variation characteristics of each segment when the cylinder spans the ISW.

Although many scholars have studied the force characteristics of the cylinder in ISWs, the number of segments of the whole cylinder is relatively small, and, in addition, the flow mechanism is rarely studied. In this study, the whole cylinder is divided into 40 equally spaced sections. The variation of the lift force and drag force of each section of the cylinder during the interaction with the ISW is studied separately. It is found that the drag force on the cylinder is 10 times higher than the lift force. It is proven that the shear phenomenon induced by the horizontal force is the main cause of the safety hazard of the structures. It is also found that the horizontal force is mainly caused by pressure, and the horizontal force induced by wall shear stress is only a small proportion. To explore the flow mechanism, we extract the main flow modes in the flow field based on the dynamic mode decomposition method. We analyze the main reasons that trigger the force distribution characteristics of the cylinder from the perspective of modes.

2. Numerical Methodology

2.1. Continuity and Momentum Equations

Based on the continuity assumption, the Navier–Stokes (N–S) equations include the conservation of mass and the conservation of momentum, which are expressed by Equations (1) and (2), respectively [13–15].

$$\frac{\partial \rho}{\partial t} + \frac{\partial (\rho u_i)}{\partial x_i} = 0 \tag{1}$$

$$\frac{\partial (\rho u_i)}{\partial t} + \frac{\partial (\rho u_i u_j)}{\partial x_j} = -\frac{\partial p}{\partial x_i} + \frac{\partial}{\partial x_j}\left(\mu \frac{\partial u_i}{\partial x_j}\right) + f_i \tag{2}$$

where ρ is the fluid density, t is the time, i (i = 1, 2, 3) is the three directions of the Cartesian coordinates, x_i is the spatial coordinate, u is the flow velocity, p is the pressure, μ is the kinematic viscosity, and f is the body force.

2.2. Turbulence Model

The SST k-ω model, while retaining its essence, was developed by building upon the standard k-ω model. By incorporating a blending function, it combines the strengths of both the k-ε and k-ω models. Specifically, the standard k-ω model is employed in close proximity to the wall boundaries, whereas the k-ε model is utilized in the boundary layer edge and fully developed flow regions. This unique approach allows the SST k-ω model to effectively handle near-wall flows. In addition, the SST k-ω model offers additional features such as the consideration of rotating reference frames and shear flows, accounting for the propagation of turbulent shear stresses. Consequently, it exhibits enhanced accuracy in simulating separation points and the sizes of separation zones induced by pressure gradients [16,17]. Its transport equations are as follows:

$$\frac{\partial}{\partial t}(\rho k) + \frac{\partial}{\partial x_i}(\rho k u_i) = \frac{\partial}{\partial x_j}\left(\Gamma_k \frac{\partial k}{\partial x_j}\right) + G_k - Y_k + S_k \tag{3}$$

$$\frac{\partial}{\partial t}(\rho \omega) + \frac{\partial}{\partial x_j}(\rho \omega u_j) = \frac{\partial}{\partial x_j}\left(\Gamma_\omega \frac{\partial \omega}{\partial x_j}\right) + G_\omega - Y_\omega + D_\omega + S_\omega \tag{4}$$

where G_k and G_ω represent the generation of the turbulent kinetic energy and dissipation, respectively. Γ_k and Γ_ω represent the effective diffusivity of k and ω, respectively. Y_k and Y_ω represent the dissipation of k and ω due to turbulence, respectively. D_ω represents the cross-diffusion term, calculated as described below. S_k and S_ω are user-defined source terms.

The numerical solution of the governing equations is accomplished through the utilization of the ANSYS Fluent 2019 commercial software. The SIMPLE algorithm is used to discretize the equations. For the gradient terms of convection and diffusion, a least-squares cell-based approach is utilized. The pressure interpolation at cell faces is carried out using the PRESTO! The second-order implicit scheme is used globally, which guarantees computational accuracy.

2.3. Modeling of Numerical Tank

To generate the ISW, we first need to build the numerical tank. In the 3D Cartesian coordinate system, the numerical tank is 12 m long, 0.8 m wide, and 0.8 m deep, as shown in Figure 1. The corresponding computational mesh structure is shown in Figure 2. In the real marine environment, along the vertical direction, it can be divided into three parts according to the density distribution. They are the upper layer, the lower layer, and the pycnocline in the middle. The density distribution of the upper and lower layers is more uniform while the density of the middle pycnocline is constantly changing along the water depth. In this paper, the density of the upper layer is 999 kg/m^3 and the depth is h_1. The density of the bottom layer is 1018.5 kg/m^3 and the depth is h_2. The density distribution in the pycnocline is specified using the hyperbolic tangent function as seen in Equation (5) [18].

In this study, we use the gravity collapse method to generate the ISWs. Specifically, a long rectangular gravitational potential well of length L and depth D was established on the left side of the tank. The gravitational collapse zone is separated from the rest of the zone by a gate. A low-density fluid is injected above the gravity collapse region, creating a height difference at the interface between the two sides of the gate. When the gate is opened, an initial disturbance in the form of a step is created. At this point, the denser fluid will sink and the lighter fluid will float under the action of gravity. Thus, the fluid below the right side moves to the left and the fluid above the left side moves to the right. This creates a restoring moment that forms an ISW. An ISW is usually unstable when it

first forms. It takes some time for the interactions between the peaks and troughs of the wave to adjust and balance, resulting in a more stable wave structure. So, the cylinder is placed in the center of the tank, which allows the ISW to stabilize for a sufficiently long period of time. This also eliminates the effects of reflected waves. The diameter of the cylinder, d, is chosen to be 0.05 m, taking into account the relative size of the actual ISW to the marine structure. In addition, the interaction of the ISW with the cylinder is an unsteady process. Therefore, we need to specify the time step in the simulation. The time step should be chosen to satisfy the Courant–Friedrichs–Lewey (CFL) stability criterion [19]. According to the CFL criterion, the distance traveled in a time step must be less than the length of a grid. ($\Delta t < \min(\Delta x/|U|, \Delta z/|W|)$, where Δt is the time step, Δx is the unit grid size in the horizontal direction, U is the horizontal velocity, Δz is the unit grid size in the vertical direction, W is the vertical velocity). In this paper, $\Delta x_{\max} = 0.02$, $\Delta z_{\max} = 0.01$, $U_{\max} = 0.09$, and $W_{\max} = 0.05$. Therefore, we choose the time step Δt = 0.01 s, which satisfies the CFL criterion.

$$\begin{cases} \rho_1 & \left(z > z_c + \frac{d_c}{2}\right) \\ \frac{\rho_1+\rho_2}{2}\left\{1 - \frac{\rho_2-\rho_1}{\rho_1+\rho_2}\tanh\left(\frac{z-z_c}{d_c}\right)\right\} & \left(z_c - \frac{d_c}{2} < z < z_c + \frac{d_c}{2}\right) \\ \rho_2 & \left(z < z_c - \frac{d_c}{2}\right) \end{cases} \quad (5)$$

where z is the vertical position, and ρ_1 and ρ_2 represent the density of the upper and lower fluids, respectively. z_c is the vertical location of the pycnocline center. The pycnocline center is obtained by calculating the gradient of the density field. The maximum value of the gradient represents the position of the center of the pycnocline. d_c is the thickness of the pycnocline.

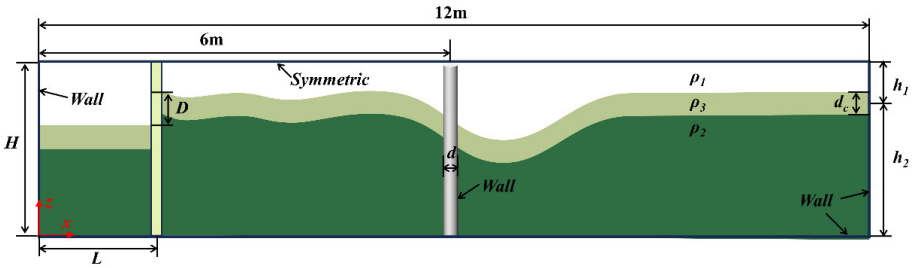

Figure 1. Schematic diagram of the numerical tank setup.

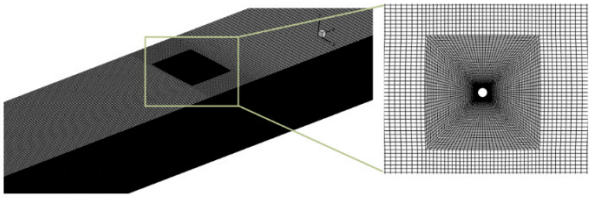

Figure 2. The computational mesh structure in the domain.

3. Model Verification

In order to avoid the interference of mesh size on the numerical simulation results, we first need to verify the mesh independence. Specifically, we used 3.08 million, 3.54 million, and 4.36 million mesh elements to represent coarse, medium, and fine configurations, respectively. Under the three mesh configurations, we computed and obtained the results of the ISW flow field generated at a collapse height of 0.1 m. We extracted the ISW troughs where the wave was located. We extract the horizontal velocity on the vertical profile where the trough of the ISW is located, and a comparison of the computational results under the three grid configurations is shown in Figure 3. We find that the horizontal velocities on the vertical line of the ISW trough computed by the three grids are essentially the same. Therefore, we use the mesh of the dense case as the mesh. This ensures the accuracy of the

numerical simulation. The above mesh-independent analysis can show the accuracy of our calculations.

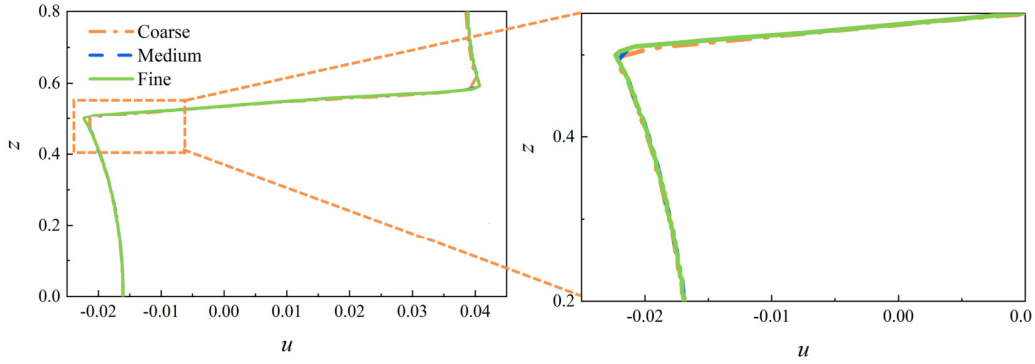

Figure 3. Horizontal velocity on the vertical line of the ISW trough for three numbers of mesh elements.

We also compared the computational and experimental results in addition to the mesh independence analysis. Du et al. [20–22] summarized the relationship between the gravity collapse coefficient S and the collapse length, height, and upper and lower layer heights in their experiments, seen in Equation (6). We compared our numerical results with their experimental results according to their settings of the relevant parameters in their experiments, seen in Figure 4. The results show that our numerical results are in general agreement with the experimental data. This shows the accuracy of our calculations.

$$S = \sqrt{\frac{1.5D(h_1 - h_2)}{h_1^2 h_2^2}} L \tag{6}$$

$$c_0 = \sqrt{gh_1h_2(\rho_2 - \rho_1)/(\rho_2 h_1 + \rho_1 h_2)} \tag{7}$$

where S represents the gravity collapse coefficient. h_1 and h_2 represent the height of the upper and lower fluids, respectively. D represents the gravity collapse height (the vertical distance between the interfaces on both sides of the gate). L represents the length of the collapse zone. c_0 is the linear long wave velocity. g is the gravitational acceleration. ρ_1 and ρ_2 represent the density of the upper and lower fluids, respectively.

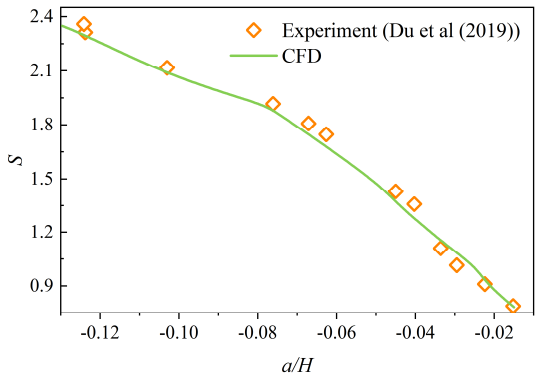

Figure 4. Comparison of generated ISW results between CFD and experimental results of Du et al. [20].

4. Results and Discussions

4.1. Evolution of the Flow Field around a Cylinder in the ISW

We created ISW flow fields with collapse heights of 0.1 m, 0.2 m, and 0.3 m, respectively, using the gravity collapse method. The velocity distributions in the horizontal direction are shown in Figure 5. Comparison reveals that the horizontal velocities induced by the ISW

are bounded by the pycnocline, and the upper and lower layers of fluid move in opposite directions. The horizontal velocity on the vertical line at the wave trough position is the largest in the whole flow field. For this reason, the horizontal velocities on the vertical line at the wave trough position for the three cases are extracted and dimensionless. The correlation curves are shown in Figure 6. In order to perform the dimensionless treatment, we introduced the linear long wave velocity c_0 as shown in Equation (7). Due to the uniform thickness of the pycnocline, the horizontal velocity of the ISW gradually increases with the increase in the collapse height h. The horizontal velocity of the ISW increases gradually. This leads to a more drastic change in the value of the velocity in the pycnocline. The analysis of the flow field here provides the basis for the following analysis of the force law of the column in the internal wave at different scales.

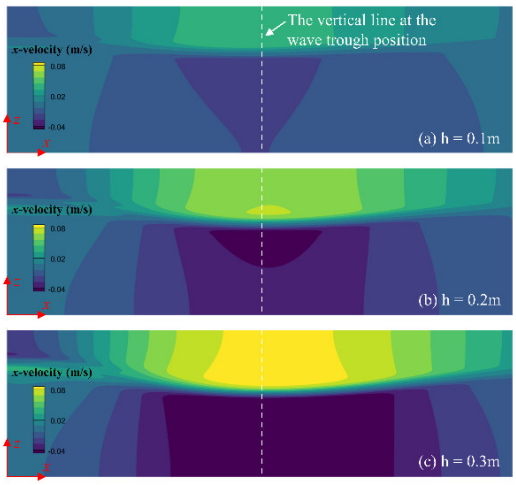

Figure 5. Velocity distribution of ISWs of different amplitudes.

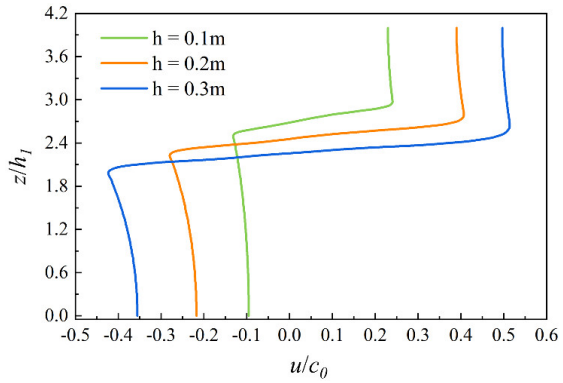

Figure 6. The horizontal velocities on the vertical line at the wave trough position.

In order to explore the evolution law of the flow field around the cylinder in the ISW, we extracted the results of the time-series flow field of the ISW interacting with the cylinder at three scales, as shown in Figure 7. We find that the ISW induces an elliptical flow field with its nucleus located at the wave trough. It rotates clockwise and moves forward. The tangential direction of the streamlines represents the direction of the velocity at the local location. Based on the orientation of the streamlines, we can see that the horizontal velocities of the upper and lower layers are opposite. At the initial stage of the contact between the ISW and the cylinder, there is almost no backflow on the backflow region of the cylinder. As time progresses, the backflow area in the backflow region gradually increases and the value of the wake velocity gradually increases. In addition, after the wave trough reaches the location of the cylinder, the cylindrical wake gradually becomes chaotic as the scale of the ISW increases. We can find from the distribution of the streamlines. In addition,

we also analyzed the change in wavefront and the distribution of shear stress on the wall of the cylinder when the ISW flows through the cylinder, as shown in Figure 8. There is a lifting phenomenon of the wavefront at the back of the cylinder. As the scale of the ISW increases and the time advances, the area of the lifted wavefront behind the cylinder increases gradually and becomes chaotic. This is the effect of the cylinder on the wave surface, and in turn, the ISW generates shear stress on the surface of the cylinder. There will be symmetrical areas of high shear stress from the flow onset point to the separation point. For the cylinders in the upper and lower layers, the wall shear stresses applied are in opposite directions. In addition, the wall shear stress distribution in the wake region gradually becomes chaotic, a behavior caused by the shedding of the wake vortex of the cylinder.

To further quantitatively analyze the variation of the cylindrical wall shear stress, we extracted the maximum value of the forward direction and the backward direction of the cylindrical wall shear stress, which are shown in Figures 9 and 10. The changes in their values reflect the extreme stress state of the cylinder. We find that both of them have the trend of gradually increasing to the maximum value and then decreasing. However, the wall shear stress in the forward direction will be higher than that in the backward direction. For example, in the case of h = 0.3 m, the peak value of wall shear stress in the forward direction is 0.214 Pa, while the peak value of wall shear stress in the backward direction is 0.139 Pa. The peak value in the forward direction is 35% higher than in the reverse direction. This is due to the difference in horizontal velocity values between the upper and lower layers of the ISW. We also find that there is a fluctuation in the value of the wall shear stress as the trough of the ISW gradually moves away from the cylinder. The greater the collapse height h, the more pronounced the fluctuation.

4.2. Force Characteristics of Cylinders in the ISW

In order to investigate the force law of the cylinder in the ISW, we divide the whole cylinder into 40 segments at equal distances along the vertical direction, and the length of each segment is 0.02 m, since the horizontal force exerted on the cylinder is the dominant factor threatening the safety of the cylinder when it interacts with the ISW. Therefore, in this paper, the horizontal force ensemble is calculated by integrating the pressure and velocity shear on the surface of the cylinder. The force on the whole cylinder can be viewed as the sum of the contribution of the force on each segment of the cylinder at the time, i.e., as the sum of the normal pressure and tangential viscous components [23].

$$\vec{F} = \sum_i -s_{f,i} P_i \vec{n}_i + \sum_i \mu s_{f,i} u_{s,i} \vec{\tau}_i \tag{8}$$

where s_f is the face area, P is the pressure, μ is the dynamic viscosity, u_s is the velocity shear at the cylinder surface, h is the distance between cylinder section and bottom boundary, $\vec{n}$ is the unit surface normal around the cylinder, and $\vec{\tau}$ is the unit tangential vector along the velocity direction.

The force on the cylinder is a time-varying process, as the ISW travels through the cylinder. We extracted the lift force F_l and drag force F_d of the cylinder, the variation of which is shown in Figures 11 and 12, where F_l is positive vertically upward and F_d is positive horizontally to the right. For F_l, it exhibits a gradual increase and then decrease in each of the up and down directions. It can be considered that the cylinder has a tendency to vibrate up and down. For F_d, the force is realized as an increase and then a decrease, and the force is always positive. It can be seen that F_d is 10 times greater than F_l. Therefore, the horizontal force on the cylinder should be more concerned for safety reasons. To analyze the force details of the cylinder, we further extracted the lift and drag forces applied to each segment of the cylinder, see Figures 13 and 14. For each segment of the cylinder, the drag force continues to be much greater than the lift force. In addition, we find that the direction of the force on each segment of the cylinder is almost the same at all times. Although some segments of the force are not in the same direction, the shear phenomenon induced by the

lift force is much weaker compared to the drag force. Therefore, for the structural safety of the cylinder in the ISW, we should pay more attention to the variation of the drag force in its horizontal direction.

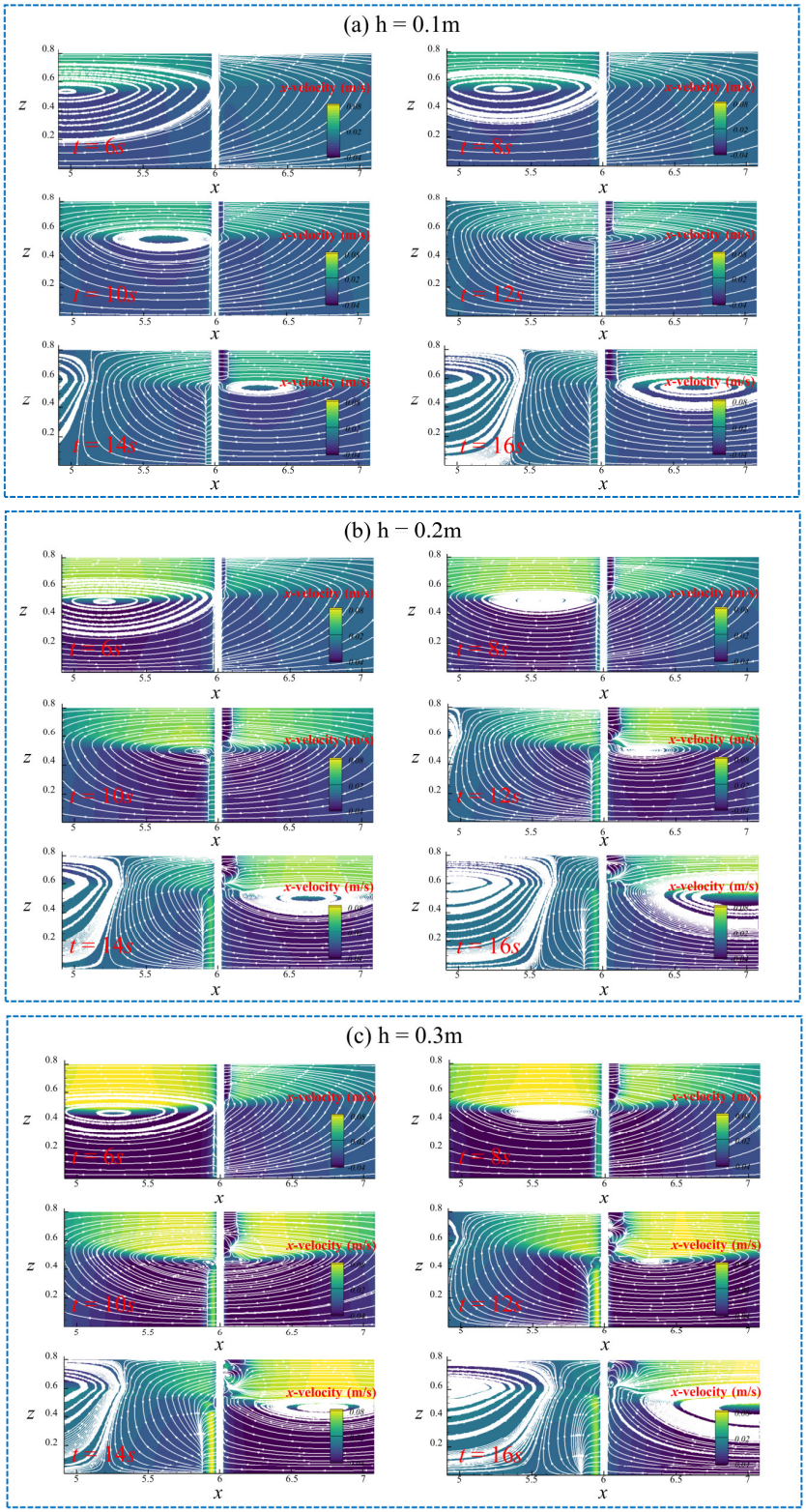

Figure 7. Horizontal velocity and streamline distribution around the cylinder at different times. (**a**–**c**) show the evolution of the flow field at different moments for gravity collapse heights of 0.1 m, 0.2 m and 0.3 m, respectively.

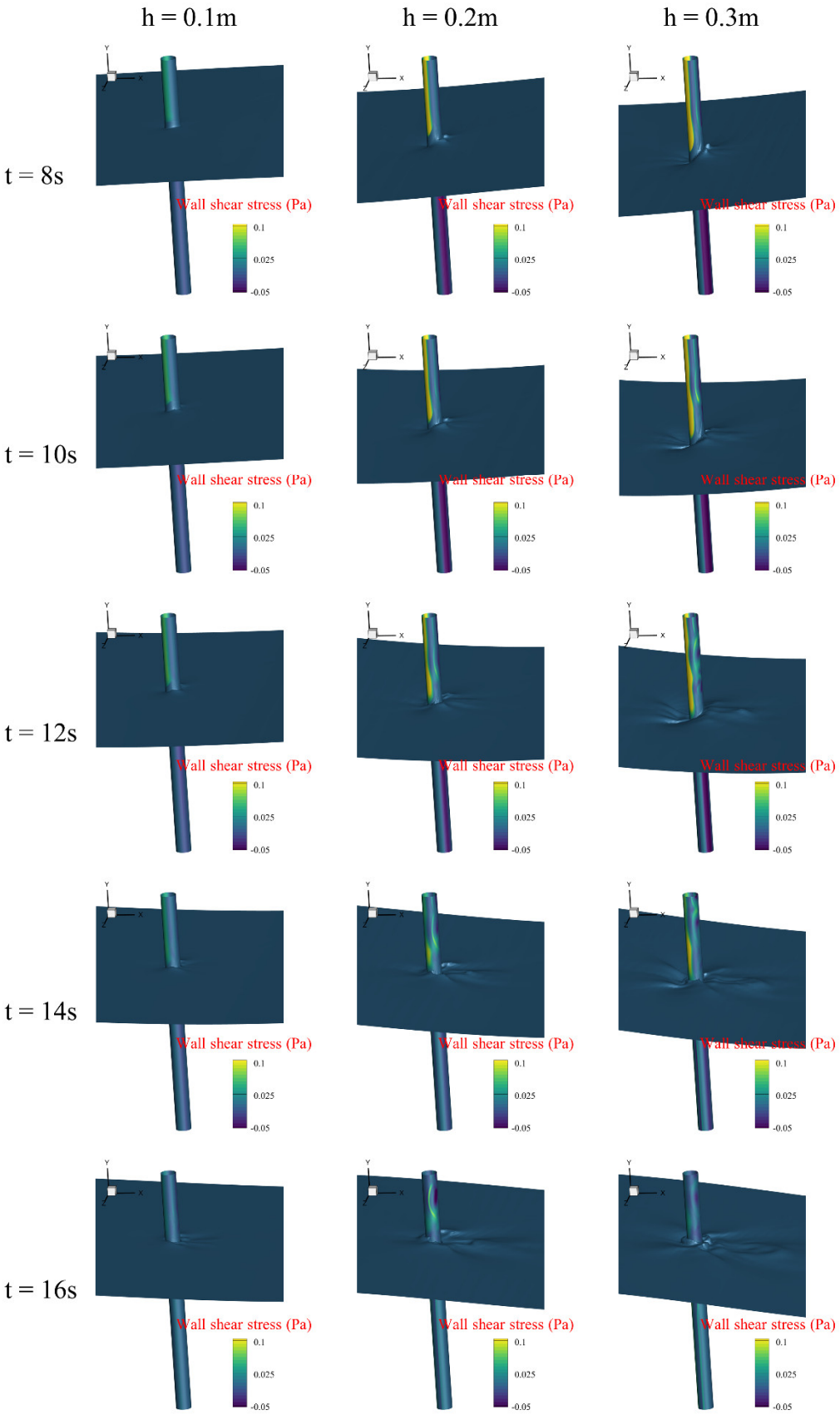

Figure 8. The change in wavefront and the distribution of shear stress on the wall of the cylinder when the ISW flows through the cylinder.

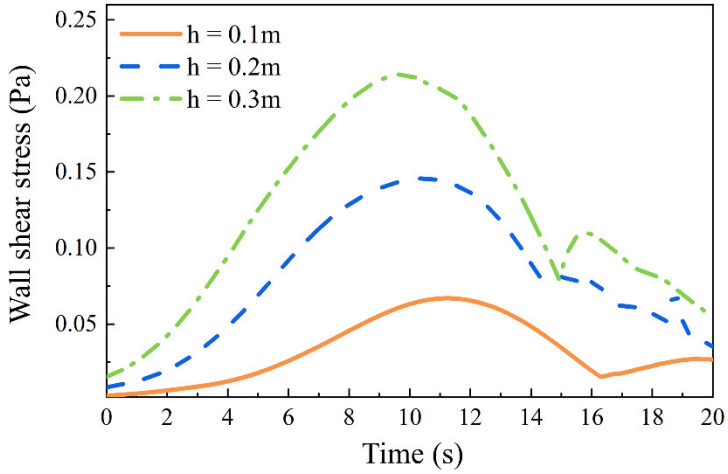

Figure 9. Maximum value of wall shear stress in the forward direction at different moments of time.

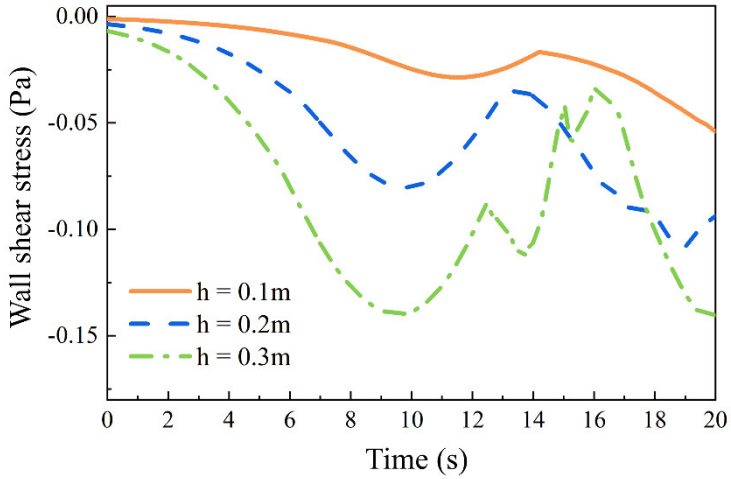

Figure 10. Maximum value of wall shear stress in the backward direction at different moments of time.

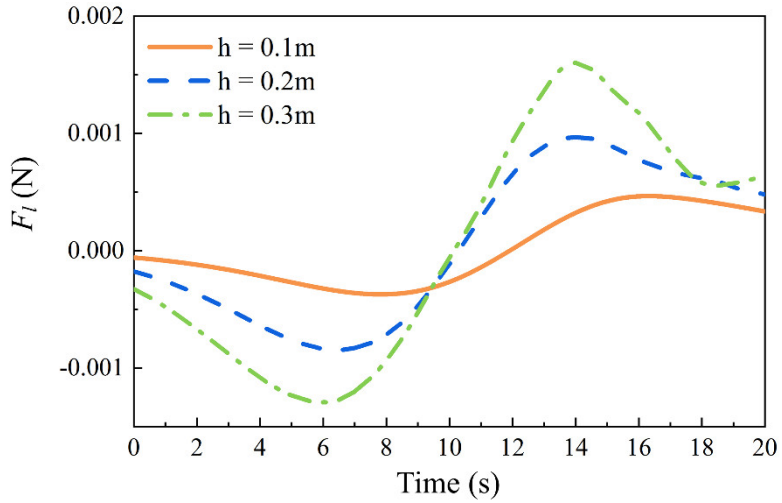

Figure 11. Lift force of the whole cylinder at different moments of time.

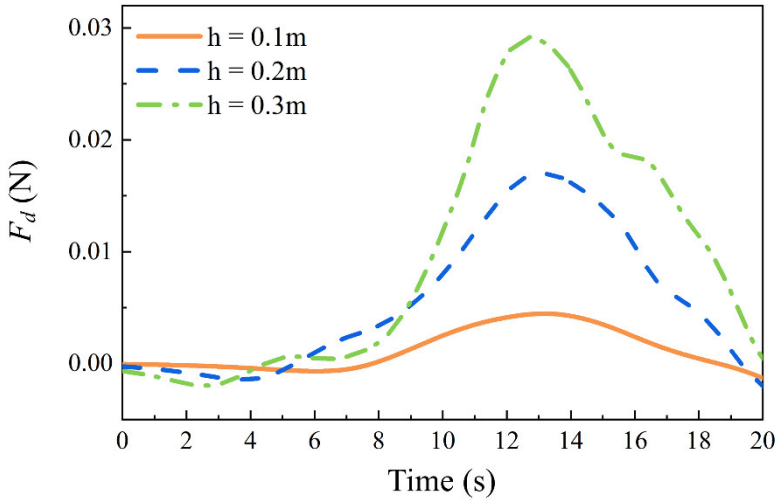

Figure 12. Drag force of the whole cylinder at different moments of time.

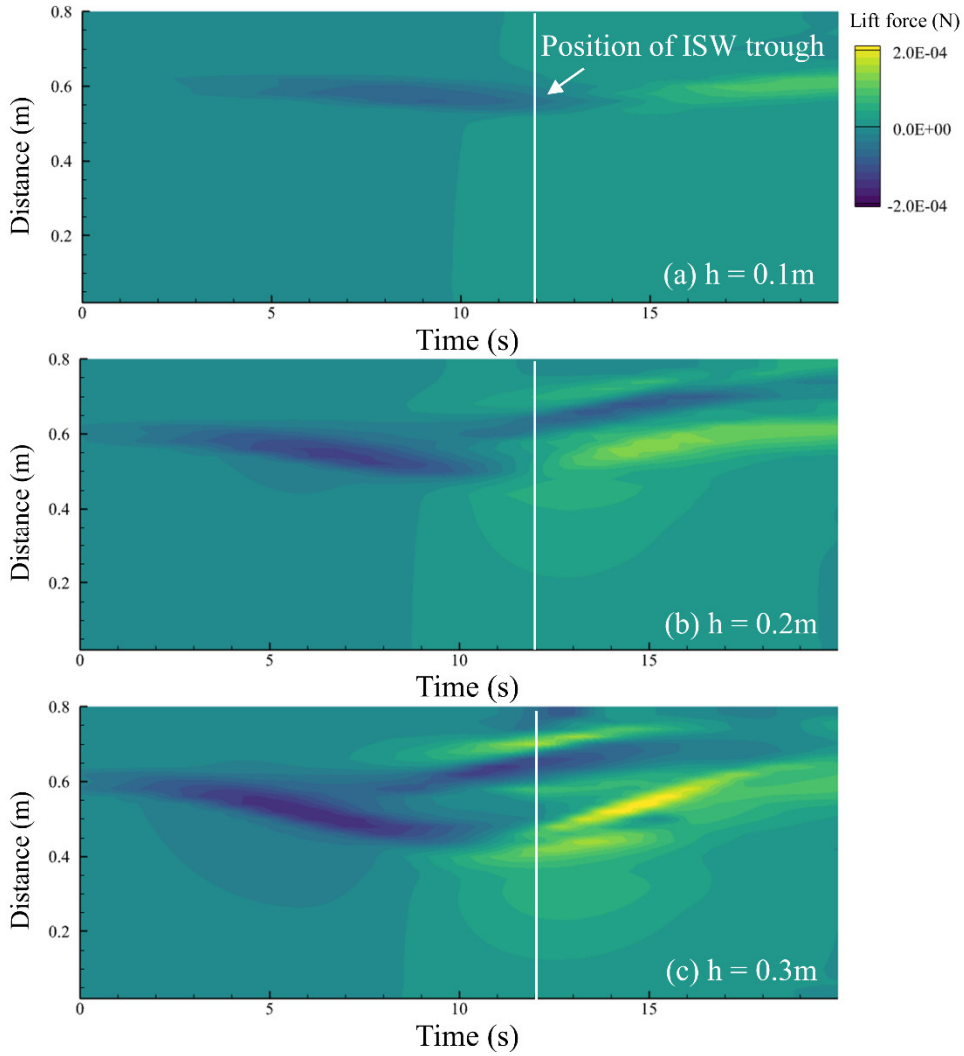

Figure 13. Lift force of each segment of the cylinder in the ISWs at different moments of time. (**a**) Lift force of each segment of the cylinder in an ISW with h = 0.1 m. (**b**) Lift force of each segment of the cylinder in an ISW with h = 0.2 m. (**c**) Lift force of each segment of the cylinder in an ISW with h = 0.3 m.

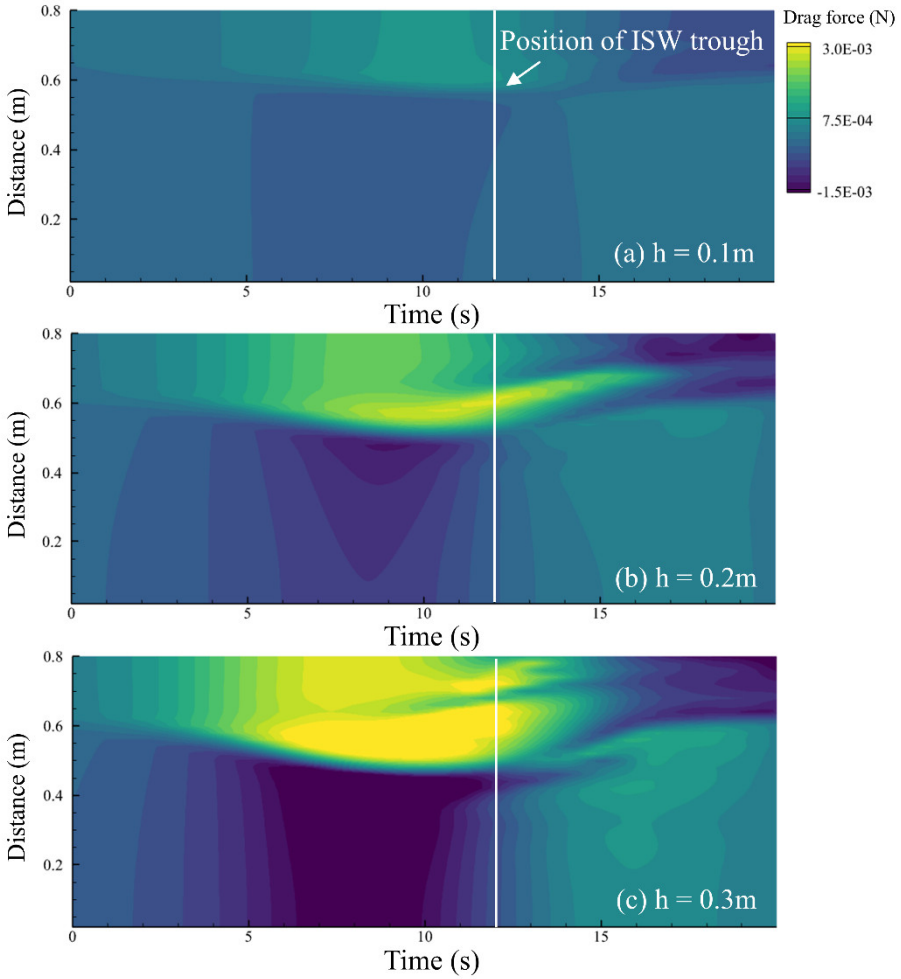

Figure 14. Drag force of each segment of the cylinder in the ISWs at different moments of time. (**a**) Drag force of each segment of the cylinder in an ISW with h = 0.1 m. (**b**) Drag force of each segment of the cylinder in an ISW with h = 0.2 m. (**c**) Drag force of each segment of the cylinder in an ISW with h = 0.3 m.

We can find that the drag forces on the cylinder are in opposite directions between the upper and lower layers as it traverses the ISW, which is bounded by the intermediate pycnocline. As the scale of the ISW becomes larger, the strength of the force on the cylinder increases. In addition, we can find that the trough of the ISW arrives at the position where the cylinder is located at t = 12 s. Therefore, the process of the cylinder travelling through the ISW can be divided into two stages: the cylinder is gradually approaching the trough from 0 to 12 s; and the cylinder is gradually moving away from the trough from 12 s to 20 s. In the first stage, the distribution of the force characteristics of the cylinder is similar to the horizontal velocity of the ISW flow field. In the second stage the horizontal force distribution becomes chaotic, and the larger the ISW scale is, the more chaotic it is.

In order to further analyze the force commonality of the cylinders under different scales of ISW, we carried out the dimensionless quantification of the horizontal force. The distribution of the horizontal force after dimensionless sizing is shown in Figure 15. In the first stage, when the scale of the ISW increases, the force on the cylinders also increases. In addition, the cylindrical forces in the upper fluid become progressively more complex with time evolution. In the second stage, the force on the cylinder in the upper fluid becomes smaller instead as the ISW scale increases. Figure 16 reflects the force behavior of the whole cylinder in the ISW. We find that the force at h = 0.2 m is consistently larger than the case of h = 0.1 m. When h = 0.3 m, the force profile of the cylinder changes more complicatedly.

Sometimes it is lower than the previous two cases, but its peak point is higher than the two, and its trend is consistent with the previous two.

$$CF^* = \frac{2F_x}{\rho_1 U_{\max}^2 DH} \tag{9}$$

where F_x is the horizontal force, ρ_1 represents the density of the upper layer, $U_{\max}$ is the maximum value of transverse velocity, D is the diameter of the cylinder, and H is the total water depth in the tank.

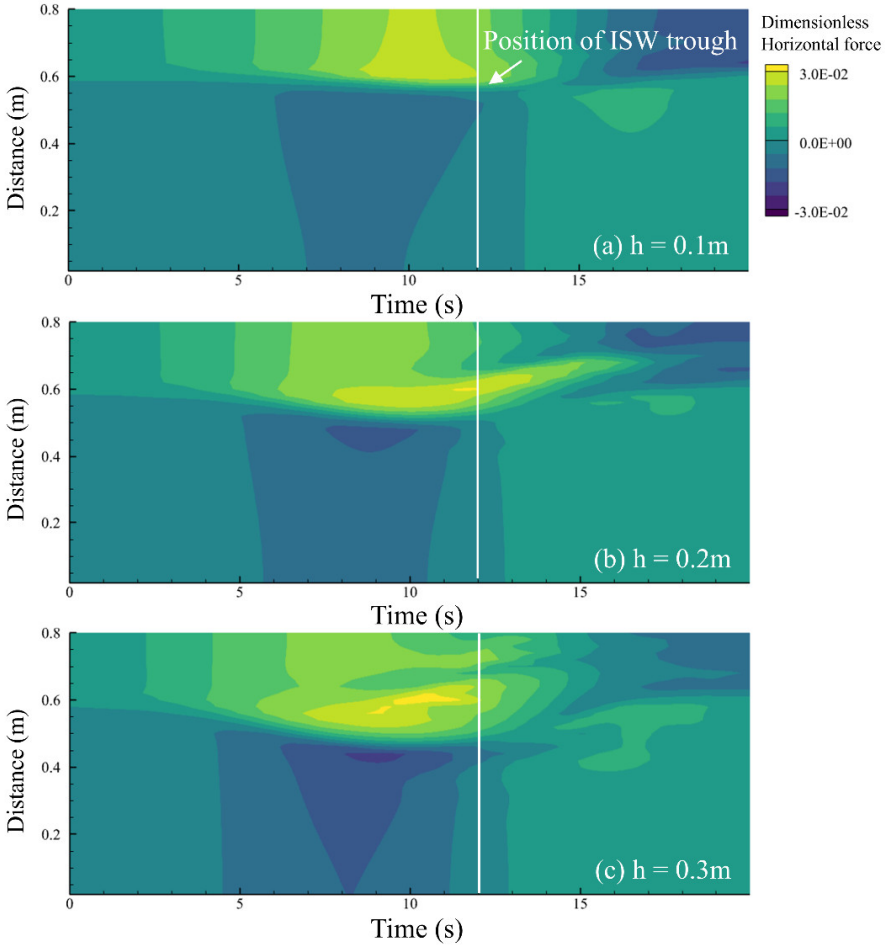

Figure 15. Temporal variation of dimensionless horizontal forces on the cylinder subjected to ISWs. (**a**) Dimensionless horizontal forces on the cylinder in an ISW with h = 0.1 m. (**b**) Dimensionless horizontal forces on the cylinder in an ISW with h = 0.2 m. (**c**) Dimensionless horizontal forces on the cylinder in an ISW with h = 0.3 m.

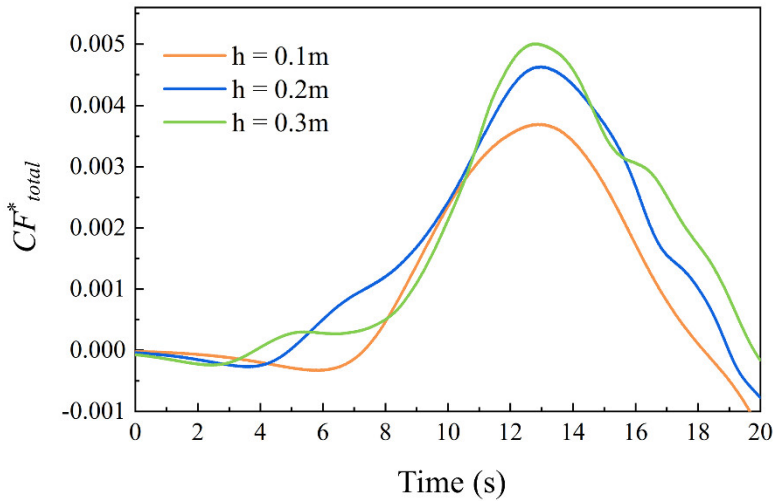

Figure 16. Temporal variation of the total combined horizontal forces of the cylinder.

In addition, we calculated the force on the cylinder under the influence of pressure to find out the specific reasons that affect the force evolution of the cylinder, as shown in Figure 17a. Figure 17b represents the total combined force, and Figure 17c represents the difference between the pressure-induced force on the cylinder and the total combined force. We use the concept of relative error as shown in Equation (10). After comparison, the share of viscous shear stress is larger when the combined force is close to zero. However, most of the time, the pressure-induced horizontal force dominates the total horizontal force. Therefore, we extracted the pressure distributions at the positions of h = 0.1 m and cylinder heights of 0.5 m and 0.7 m. The height of 0.5 m corresponds to the lower part of the pycnocline, and 0.7 m is located in the upper part of the pycnocline. In this way, we can analyze the pressure variations of the cylinder as it traverses the ISW. For the first stage, we show the pressure distribution at four moments, t = 4 s, 6 s, 8 s, and 10 s, as shown in Figure 18. The value of the pressure on the walls of the cylinders gradually increases from the beginning of the contact of the cylinder with the ISW to the trough until the arrival of the cylinder at the trough position. The pressure on the upper cylinder is greater than that on the lower one. This is because the horizontal velocity field induced by the ISW is different in magnitude between the upper and lower layers. In addition, we can also find that the pressure extremes appear near the flow separation point on the headward side. The pressure values in the separation zone on the backflow side of the cylinder also increase gradually with time. When the cylinder reaches the trough, the evolution of the pressure distribution on its wall is shown in Figure 19. We can see that the pressure on the head side is gradually weakened, and the pressure on the back side is gradually strengthened. When t = 16 s, the pressure on the backflow surface has exceeded the pressure on the onflow surface. At this time, the direction of the horizontal force on the cylinder is reversed. Thereafter, the pressure on the backflow surface continues to increase, which leads to a consequent increase in the horizontal force on the cylinder.

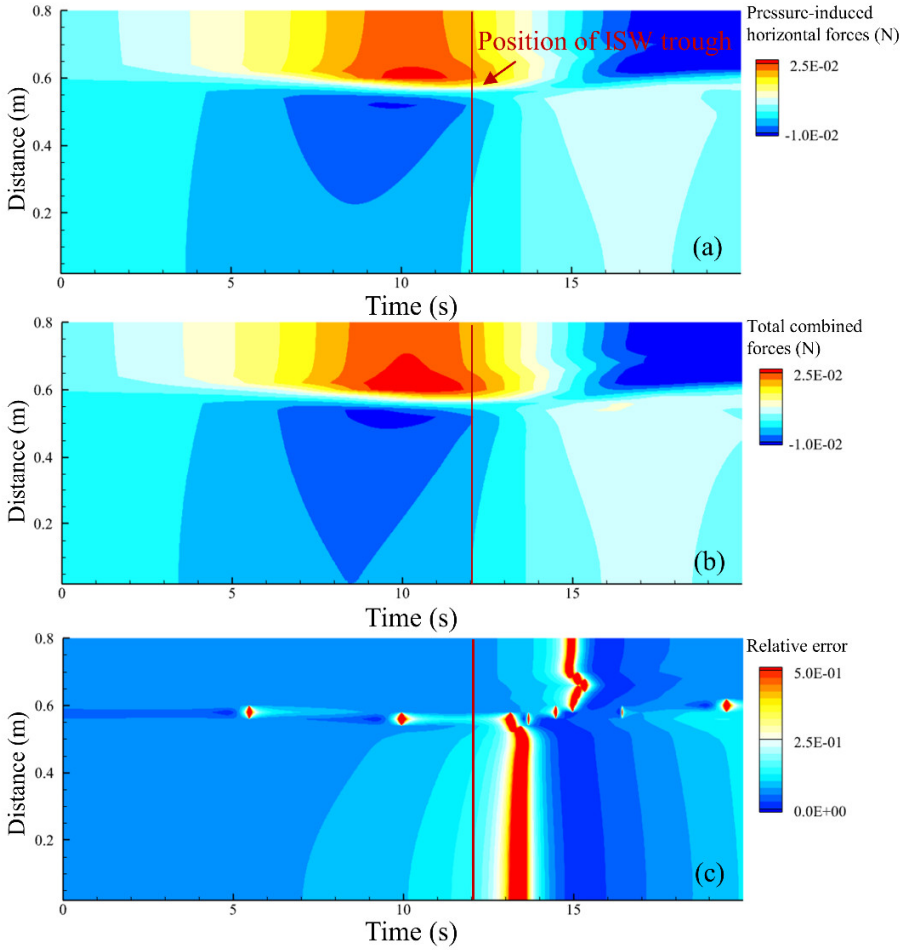

Figure 17. Pressure-induced horizontal forces versus total combined forces. (**a**) Pressure-induced horizontal forces. (**b**) Total combined forces. (**c**) The difference between the pressure-induced force and the total combined forces.

$$RE = \left| \frac{F_{xP} - F_x}{F_x} \right| \tag{10}$$

where RE represents relative error, F_x is the horizontal force, and F_{xp} is the pressure-induced horizontal force.

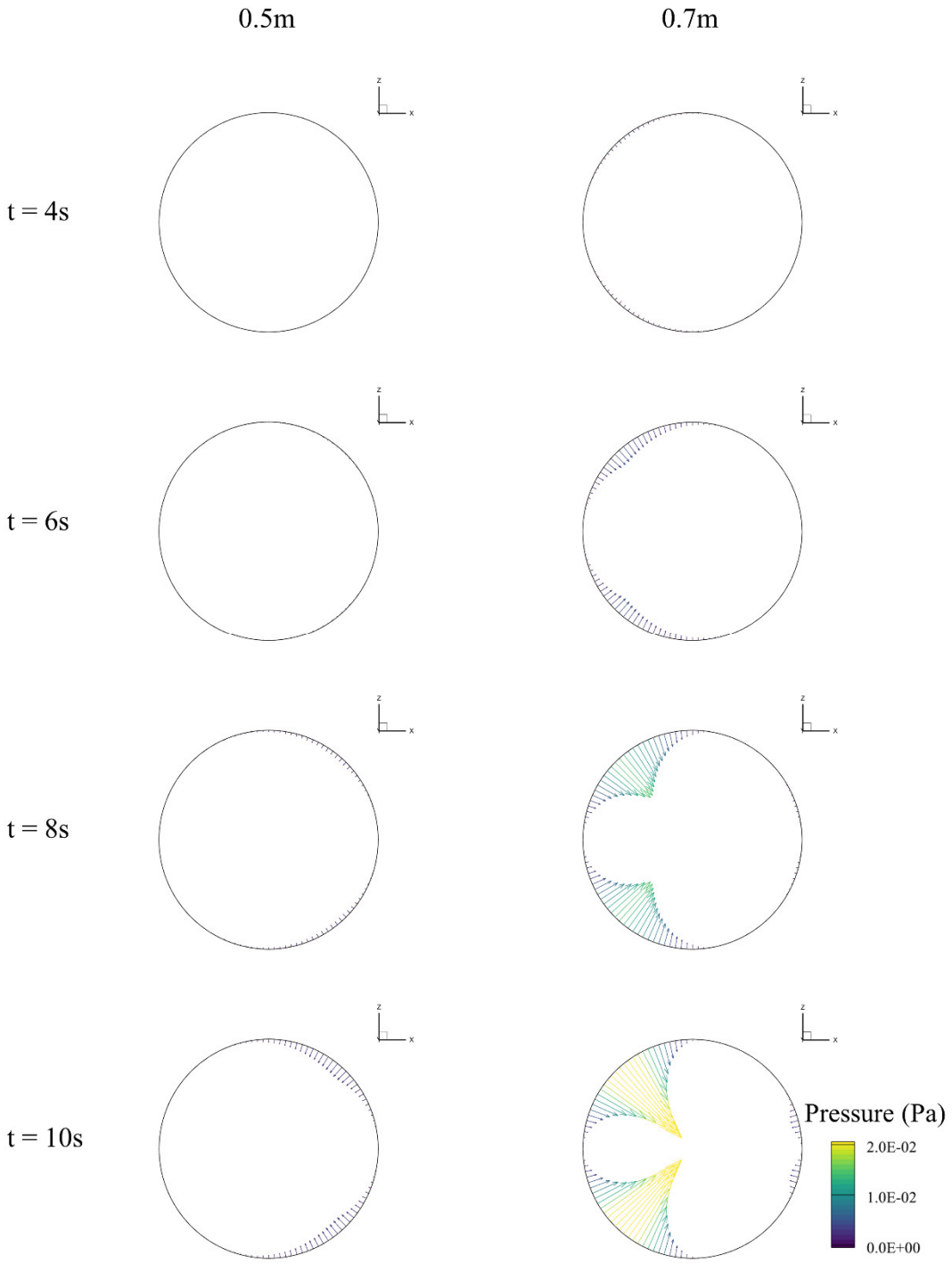

Figure 18. Dynamic pressure changes on a cylinder as the trough of the ISW gradually approaches.

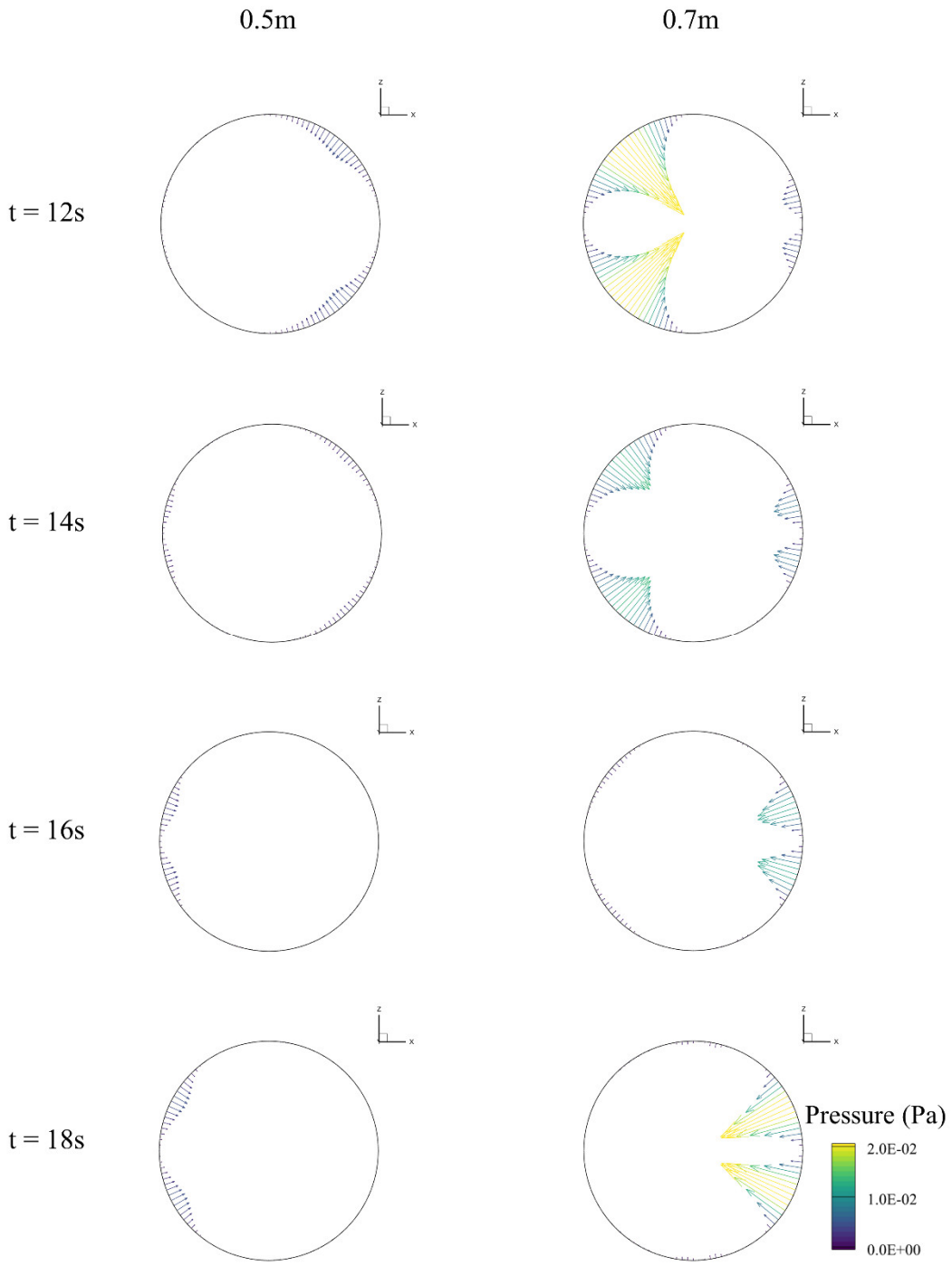

Figure 19. Dynamic pressure changes on the cylinder as the trough of the ISW gradually moves away from it.

4.3. Spatiotemporal Evolution Patterns of Cylindrical Trailing Vortex

In the above article, we found that the horizontal force on the cylinder will show a certain pattern of change when it crosses the ISW. Previous studies have also shown that the force on the cylinder is closely related to the shedding phenomenon of its wake [24]. Therefore, we try to analyze the force characteristics of the cylinder from the evolution characteristics of the cylindrical trailing vortex. We adopt the dynamic mode decomposition (DMD) method to extract the main modes. These main modes represent the dominant flow structure in the whole time period [25]. The intrinsic flow of information can be mined by analyzing its spatial and temporal evolution.

Before using the DMD method, multiple snapshots of time over a period of time must be integrated into a two-dimensional matrix [26]. The complete time snapshot matrix is then divided into two matrices, $\mathbf{X}\,\mathbf{X}'$,.

$$\begin{array}{ll} \mathbf{X} = & [\mathbf{x}_1 \quad \mathbf{x}_2 \quad \ldots \quad \mathbf{x}_{m-1}] \\ \mathbf{X}' = & [\mathbf{x}_2 \quad \mathbf{x}_3 \quad \ldots \quad \mathbf{x}_m] \end{array} \tag{11}$$

Assuming that $\mathbf{x}$ is linearly correlated with $\mathbf{X}'$, we can obtain the matrix A. The A matrix can be calculated by eigendecomposition $\mathrm{A}\Phi = \Phi\Lambda$. This step is obtained based on the low-rank approximation of the data matrix.

$$\mathbf{X}' = \mathbf{A}\mathbf{X} \tag{12}$$

Eigenvalues and eigenvectors are obtained utilizing rank truncation. These eigenvalues move forward in time. The state at each time in the original data can be calculated by the linear combination of DMD modes (columns ϕ_k of $\mathbf{\Phi}$), eigenvalues ($\lambda_k = \Lambda_{kk}$), and corresponding modal amplitudes b:

$$\mathbf{x}(t) = \sum_{k=1}^{r} b_k \phi_k(\xi) \exp(i\omega_k t) \tag{13}$$

In this study, the interaction of ISWs with the cylinder is an unsteady process. Therefore, we selected 2000 snapshots. The time interval between two snapshots is 0.01 s. The total duration is 20 s. In addition, we found that the trough of the ISW arrives at the location of the cylinder at t = 12 s. Therefore, the whole flow field is divided into two segments with t = 12 s as discontinuity. For the first segment, we extracted the cylindrical trailing vortex modes in three scales of ISWs. The lower the corresponding frequency of the mode, the higher the energy contributed. That is, the order of frequencies determines the order of modes. For the trailing vortex field around the cylinder under the influence of the three scaled ISWs, we extract the first three orders of the modes.

In Figure 20, we have extracted two vortex equivalent surfaces for $\omega_y = -0.008$ and $\omega_y = 0.008$, respectively, to demonstrate their tailing vortex patterns. The corresponding time evolution curves for each mode are shown in Figure 21. By comparing the mode 1 distributions for the three cases, it can be seen that the tailing vortex of the cylinder gradually grows as the ISW scale increases. However, as the ISW scale continues to increase, the distribution of the tailing vortex in the upper layer of the cylinder becomes irregular. The time evolution curves also show that the intensity of the tailing vortex gradually increases when the cylinder is close to the wave trough. The larger the ISW scale, the stronger and faster the intensity of the tailing vortex grows. This can also be compared to the force behavior of the cylinder, see Figure 14. In the first stage, as the ISW scale gradually increases, the force of the cylinder also increases and becomes chaotic. We can also see that the gradient of the change in force increases. For modes 2 and 3, they represent the higher frequency features of the flow field compared to mode 1, and the distribution of mode 2 is similar to that of mode 1. Mode 3 represents the smaller vortexes in the flow field, which are more complex than the first two modes. However, its total energy content is much smaller than that of the first two modes. In addition, according to the time evolution curves, it is found that the amplitude change in the corresponding modes is proportional to the scale of the internal wave. Moreover, the frequencies of the corresponding modes are almost the same under the three working conditions.

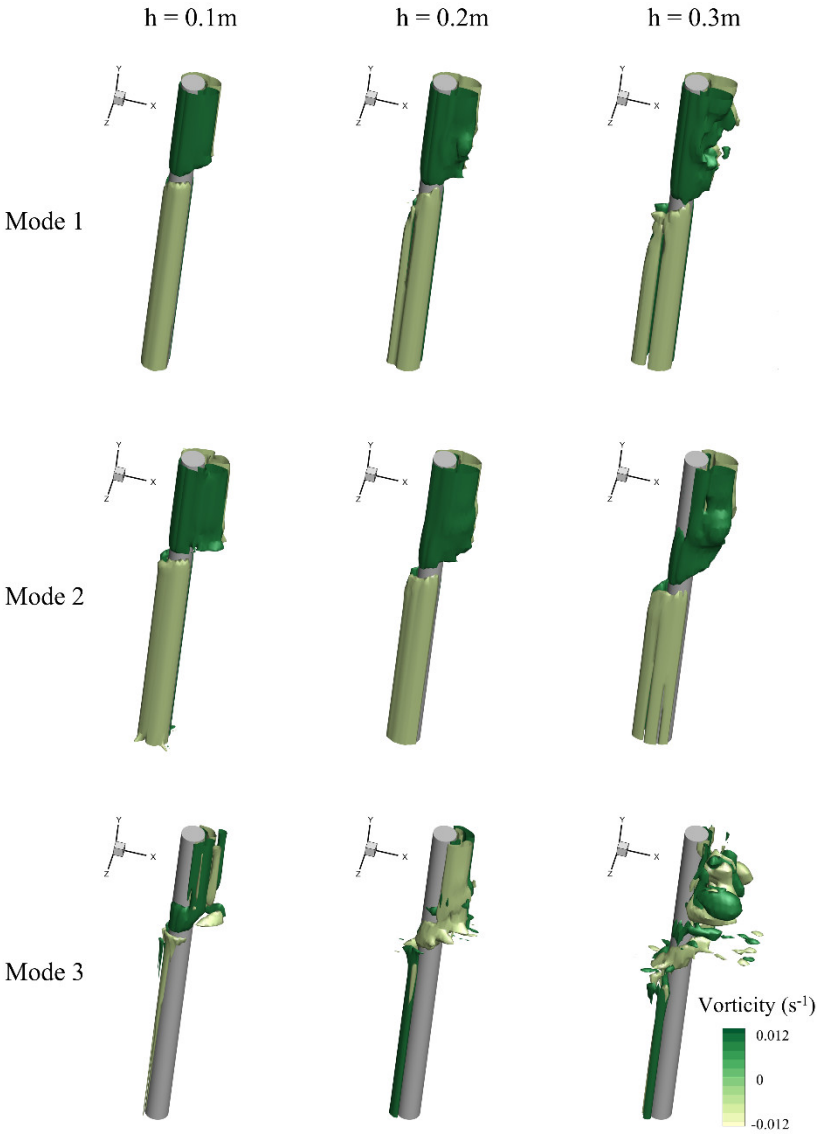

Figure 20. Mode distribution of vorticity around the cylinder in the first stage.

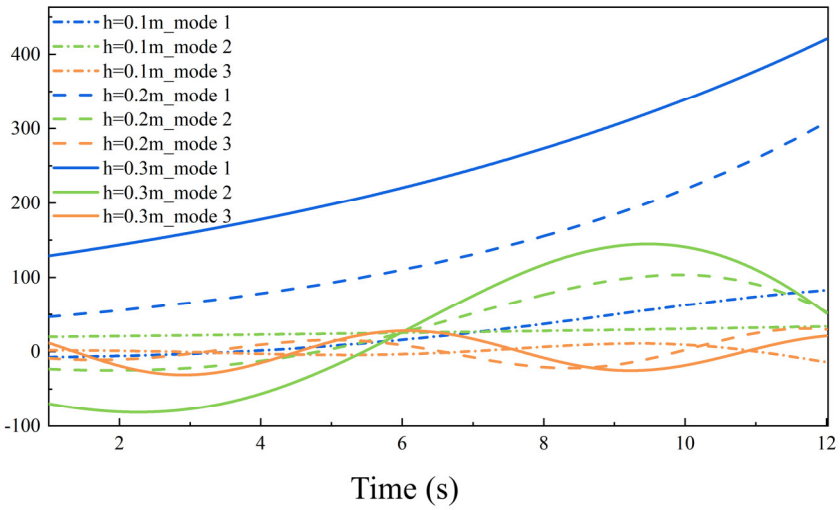

Figure 21. Time evolution of different modes in the first stage.

For the second stage in which the trough gradually moves away from the cylinder, we similarly extracted the first three orders of modes of the cylindrical trailing vortex during this process, which are shown in Figure 22. The time evolution curves corresponding to each mode are shown in Figure 23. Upon comparison, it is found that the trend of the evolution of the corresponding modes in this phase is exactly opposite to that of the first phase. In addition, the modal distribution of the vorticity in this stage is very different from that of the first stage. Taking mode 1 as an example, the wake of the cylinder in the upper layer gradually becomes chaotic when the trough gradually moves away from the cylinder. In terms of time evolution, the change in mode 1 is exactly opposite to the first stage, which is gradually weakened, and the final value comes to the same. And the larger the ISW is, the stronger the corresponding mode strength is at the same moment, the more it decreases. The above changes in the cylindrical tailing vortex can exactly confirm the force manifestation of the cylinder in the second stage in Figure 17. The force distribution of the part of the cylinder in the upper layer also becomes cluttered with the increase in the ISW scale. Comparing the performances of the first three stages of modes, we find that the cylinder can still maintain a stable vortex shedding in the ISW generated at h = 0.1 m. By the time h = 0.2 m, the vortex shedding of the cylinder becomes extremely unstable. Until h = 0.3 m, almost no stable vortex shedding appears. This is something we can analyze against from the dimensionless horizontal force distribution, as shown in Figure 15.

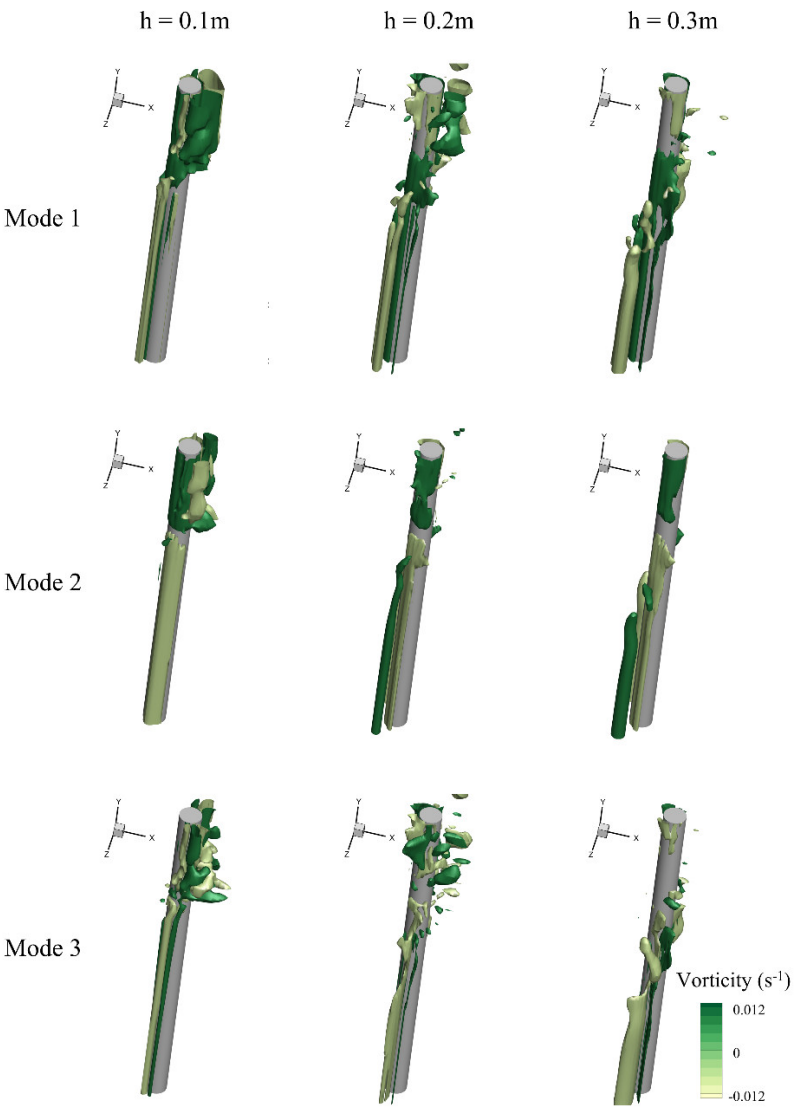

Figure 22. Mode distribution of vorticity around the cylinder in the second stage.

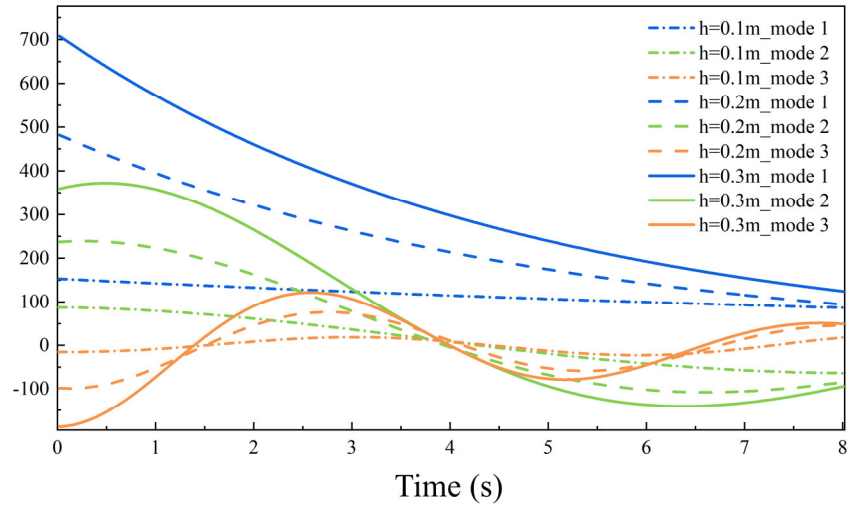

Figure 23. Time evolution of different modes in the second stage.

5. Conclusions

In this paper, we generate different scales of ISWs based on the gravity collapse method and analyze the evolution of the flow field around a cylinder. It was found that the flow field induced by the ISW is an elliptical, clockwise-rotating flow field. Its flow core is located in the intermediate pycnocline. The ISW flow field is bounded by the pycnocline, and the upper and lower layers of fluid move in opposite directions. As a result, there will be a symmetric region of high shear stress from the flow meeting point to the separation point, and the forces in the upper and lower layers are in opposite directions. With time, the wall shear stresses in the wake region of the cylinder gradually become chaotic.

In order to investigate the force pattern of the cylinder in the ISW, the whole cylinder is divided into 40 segments at equal distances along the vertical direction. The horizontal force ensemble is calculated by integrating the pressure and velocity shear on the surface of the cylinder. Through our analysis, we found that the force distribution pattern of the cylinder is consistent with the horizontal velocity of the ISW at the stage when the wave trough is gradually approaching the cylinder. In the latter half of the stage, the force gradually becomes chaotic as the cylindrical tailing vortex grows and breaks up. The larger the scale of the ISW, the more complicated the forces behave. In addition, we demonstrated that the normal pressure dominates in the total ensemble force, and analyzed the pressure changes on the cylindrical wall in different stages.

Finally, we extracted the main flow modes in each of the two stages based on the dynamic mode decomposition. When the ISW scale increased, we analyzed the change in the trailing vortex flow field of the cylinder in terms of the mode distribution as well as its time evolution. In addition, we analyzed the flow characteristics in the two phases to further reveal the change in the flow state as the cylinder crosses the wave trough. More importantly, we used the flow modes to explain the reasons affecting the force performance of the cylinder.

Author Contributions: Conceptualization, M.Z. and H.H.; methodology, M.Z.; software, P.D.; validation, M.Z. and H.H.; formal analysis, M.Z.; investigation, M.Z.; resources, M.Z.; data curation, M.Z.; writing—original draft preparation, M.Z.; writing—review and editing, P.D. and A.O.; visualization, P.D.; supervision, P.D.; project administration, X.H.; funding acquisition, L.X. All authors have read and agreed to the published version of the manuscript.

Funding: This research was supported by the National Natural Science Foundation of China (No. 52201380), Fundamental Research Funds for the Central Universities (No. D5000230080), Capability Support Program of Shaanxi (No. 2024ZC-KJXX-081) and Innovation Foundation for Doctor Dissertation of Northwestern Polytechnical University (No. CX2024049).

Institutional Review Board Statement: Not applicable.

Informed Consent Statement: Not applicable.

Data Availability Statement: Data are contained within the article.

Conflicts of Interest: Author Peng Du was employed by the company Xi'an Tianhe Defense Technology Co., Ltd. The remaining authors declare that the research was conducted in the absence of any commercial or financial relationships that could be construed as a potential conflict of interest.

References

1. Bourgault, D.; Galbraith, P.S.; Chavanne, C. Generation of internal solitary waves by frontally forced intrusions in geophysical flows. *Nat. Commun.* **2016**, *7*, 13606. [CrossRef] [PubMed]
2. Zhang, M.; Hu, H.; Du, P.; Chen, X.; Li, Z.; Wang, C.; Cheng, L.; Tang, Z. Detection of an internal solitary wave by the underwater vehicle based on machine learning. *Phys. Fluids* **2022**, *34*, 115137. [CrossRef]
3. Cheng, M.H.; Hwang, R.R.; Hsieh, C.M. Numerical study on the transformation of an internal solitary wave propagating across a vertical cylinder. *Appl. Ocean Res.* **2020**, *95*, 102016.
4. Wei, G.; Du, H.; Xu, X.H.; Zhang, Y.M.; Qu, Z.Y.; Hu, T.Q.; You, Y.X. Experimental investigation of the generation of large amplitude internal solitary wave and its interaction with a submerged slender body. *Sci. China Phys. Mech. Astron.* **2014**, *57*, 301–310. [CrossRef]
5. Wang, F.; Guo, H.Y.; Li, M.L.; Meng, F.S. Experimental study on ocean internal wave force on vertical cylinders in different depths. *China Ocean Eng.* **2016**, *30*, 459–468. [CrossRef]
6. Wang, Y.; Wang, L.L.; Ji, Y.; Zhang, J.; Xu, M.; Xia, X.; Wang, C.L. Research on the force mechanism of two tandem cylinders in a stratified strong shear environment. *Phys. Fluids* **2022**, *34*, 053308. [CrossRef]
7. Cai, S.Q.; Long, X.M.; Wang, S.G. Forces and torques exerted by internal solitons in shear flows on cylindrical piles. *Appl. Ocean Res.* **2008**, *30*, 72–77. [CrossRef]
8. Song, Z.J.; Teng, B.; Gou, Y.; Lu, L.; Shi, Z.M.; Xiao, Y.; Qu, Y. Comparisons of internal solitary wave and surface wave actions on marine structures and their responses. *Appl. Ocean Res.* **2011**, *33*, 120–129. [CrossRef]
9. Lü, H.B.; Xie, J.S.; Xu, J.X.; Chen, Z.W.; Liu, T.Y.; Cai, S.Q. Force and torque exerted by internal solitary waves in background parabolic current on cylindrical tendon leg by numerical simulation. *Ocean Eng.* **2016**, *114*, 250–258. [CrossRef]
10. Si, Z.S.; Zhang, Y.L.; Fan, Z.S. A numerical simulation of shear forces and torques exerted by large-amplitude internal solitary waves on a rigid pile in South China Sea. *Appl. Ocean Res.* **2012**, *37*, 127–132. [CrossRef]
11. Wang, F.; Sun, R.; Wang, C.X.; Fu, Q.; Li, P.; Guo, H.Y. Experimental study on flow field induced by internal solitary wave and load characteristics on pile sections at different depth. *Ocean Eng.* **2019**, *188*, 106292. [CrossRef]
12. Yu, W.; Wang, F.G.; Lin, J.G.; Li, D. Numerical Simulation of the Force Acting on the Riser by Two Internal Solitary Waves. *Appl. Sci.* **2022**, *12*, 4873. [CrossRef]
13. Xie, Z.L.; Jiao, J.; Zhao, B.; Xu, F.C. Theoretical and experimental research on the effect of bi-directional misalignment on the static and dynamic characteristics of a novel bearing. *Mech. Syst. Signal Process.* **2024**, *208*, 111041. [CrossRef]
14. Jiao, J.L.; Chen, Z.W.; Xu, S. CFD-FEM simulation of water entry of aluminium flat stiffened plate structure considering the effects of hydroelasticity. *Brodogradnja* **2024**, *75*, 75108. [CrossRef]
15. Gong, S.K.; Gao, J.L.; Mao, H.F. Investigations on fluid resonance within a narrow gap formed by two fixed bodies with varying breadth ratios. *China Ocean Eng.* **2023**, *37*, 962–974.
16. Qi, C.; Lyu, X.J.; Wang, X.; Ye, H.; Shi, H.J.; Wan, Z.H. Experimental and numerical studies on vertical water entry of a cylinder under the influence of current. *Phys. Fluids* **2024**, *36*, 033322. [CrossRef]
17. Liu, S.; Ong, M.C.; Obhrai, C.; Gatin, I.; Vukčević, V. Influences of free surface jump conditions and different k− ω SST turbulence models on breaking wave modelling. *Ocean Eng.* **2020**, *217*, 107746. [CrossRef]
18. Zhang, M.; Hu, H.B.; Guo, B.B.; Liang, Q.Y.; Zhang, F.; Chen, X.P.; Xie, Z.L.; Du, P. Predicting shear stress distribution on structural surfaces under internal solitary wave loading: A deep learning perspective. *Phys. Fluids* **2024**, *36*, 035153.
19. Shiau, Y.H.; Peng, Y.F.; Hwang, R.R.; Hu, C.K. Multistability and symmetry breaking in the two-dimensional flow around a square cylinder. *Phys. Rev. E* **1999**, *60*, 6188–6191. [CrossRef]
20. Du, H.; Wei, G.; Wang, S.D.; Wang, X.L. Experimental study of elevation-and depression-type internal solitary waves generated by gravity collapse. *Phys. Fluids* **2019**, *31*, 102104. [CrossRef]
21. Peng, P.; Du, H.; Wei, G.; Wang, S.D.; Xuan, P.; Cai, S.Q.; Xie, J.S. Experimental investigation on the vertical structure characteristics of internal solitary waves. *J. Mar. Sci. Eng.* **2022**, *10*, 1045. [CrossRef]
22. Wang, S.D.; Du, H.; Wei, G.; Peng, P.; Xuan, P. Experimental modification of the internal solitary wave force exerted on a horizontal transverse cylinder due to wave-flow and vortex shedding. *Ocean Eng.* **2023**, *269*, 113513. [CrossRef]
23. Lin, Z. Numerical study on the forces and moments on a bottom-mounted cylinder by internal solitary wave. *J. Fluids Struct.* **2023**, *121*, 103952. [CrossRef]
24. Janocha, M.J.; Yin, G.; Ong, M.C. Modal analysis of wake behind stationary and vibrating cylinders. *J. Offshore Mech. Arct. Eng.* **2021**, *143*, 041902. [CrossRef]

25. Min, G.; Jiang, N. Data-driven identification and pressure fields prediction for parallel twin cylinders based on POD and DMD method. *Phys. Fluids* **2024**, *36*, 02361. [CrossRef]
26. Zhang, J.M.; Zou, L.; Sun, T.Z.; Wen, Z.H.; Yu, Z.B. Experimental investigation on the propagation characteristics of internal solitary waves based on a developed piecewise dynamic mode decomposition method. *Phys. Fluids* **2020**, *32*, 082102. [CrossRef]